Please check the marked (■) text passages carefully.

Rodrigo Soto[1,2,*]
Nuray Oktar[3]
Carles Fité[2]
Eliana Ramirez[2]
Roger Bringué[2]
Javier Tejero[2]

Experimental Study on the Liquid-Phase Adsorption Equilibrium of *n*-Butanol over Amberlyst™15 and Contribution of Diffusion Resistances

This work investigates the liquid-phase adsorption of *n*-butanol on Amberlyst™15 in the temperature range 295–323 K at different initial adsorbate concentrations. The adsorbent was characterized by N_2 physisorption, Fourier transform infrared adsorption of pyridine, scanning electron microscopy, and powder X-ray diffraction. The data obtained confirmed an adsorbent structure with two porosity levels and amorphous polymer structure. The active sites in Amberlyst™15 are of Brønsted or Brønsted-Lewis type. The liquid-phase adsorption equilibrium constants were determined at different temperatures from slurry adsorber experiments. The thermodynamic state functions were estimated and are consistent thermodynamically with physical adsorption. The macropore diffusion coefficients of *n*-butanol on Amberlyst™15 were estimated by using the moment technique, and the contribution of surface diffusion to the macropore diffusion coefficients was evaluated.

Supporting Information available online

Keywords: Adsorption, Amberlyst™15, Butanol, Diffusion resistance, Moment technique

Received: May 13, 2021; *revised:* August 09, 2021; *accepted:* August 27, 2021

DOI: 10.1002/ceat.202100253

1 Introduction

The relentless exploitation of oil reserves, which cannot be restocked in the medium or short term, and the increasing severity of legislation to reduce environmental impact have increased the use of green chemicals to replace fuels derived from oil and to be a source of platform and fine chemicals. In this framework, the blending of tertiary alkyl ethers [1], linear ethers [2], and biomass-derived esters [3] to gasoline and diesel fuels is a well-known effective alternative to improve the energetic efficiency of transportation fuels while reducing the harmful environmental impact of their combustion. This is a short-term effective way to reduce greenhouse emissions and to accomplish the legislation objectives established, e.g., by the Paris Agreement and the 2050 long-term strategy in Europe [4].

Tertiary alkyl ethers such as methyl *tert*-butyl ether, ethyl *tert*-butyl ether, *tert*-amyl methyl ether, and *tert*-amyl ethyl ether have been extensively studied. More recently, propyl *tert*-butyl ether and butyl *tert*-butyl ether have also been considered as promising gasoline additives [5, 6]. With regard to linear ethers, either symmetric or asymmetric, those with C_8–C_{16} carbon length chain, e.g., di-*n*-butyl ether [2], di-*n*-pentyl ether [7], ethyl hexyl ether [8], ethyl octyl ether, and di-*n*-octyl ether [9], are suitable additives for diesel formulations. Tertiary alkyl ethers are usually synthesized by the addition of alcohols to tertiary olefins, whereas linear ethers are typically produced from dehydration reactions of primary alcohols. Etherification reactions of glycerol with C_4 and C_5 isoolefins [10–12] and of glycerol with ethanol [13] and *tert*-butyl alcohol [14] have opened additional windows for using new oxygenates. Esters resulting from alcohol esterification with ketoacids originating from cellulose degradation, e.g., butyl or ethyl levulinate from levulinic acid and *n*-butanol [15] or ethanol [16, 17], are attractive as potential second-generation biofuels and as platform chemicals in the development of other fine chemicals, such as biosurfactants and biolubricants [18]. These chemical reactions require the presence of an alcohol as reactant and an acid catalyst to obtain a profitable product yield. Alcohols of different types and structures, e.g., primary,

[1]Rodrigo Soto
Synthesis and Solid State Pharmaceutical Centre (SSPC), Department of Chemical and Environmental Sciences, University of Limerick, Limerick, V94 T9PX, Ireland.

[2]Rodrigo Soto, Carles Fité, Eliana Ramirez, Roger Bringué, Prof. Dr. Javier Tejero
r.soto@ub.edu
Department of Chemical Engineering and Analytical Chemistry, University of Barcelona. Marti i Franqués 1-11, 08028, Barcelona, Spain.

[3]Prof. Dr. Nuray Oktar
Department of Chemical Engineering, Gazi University, Ankara, 06570 Maltepe, Turkey.

tertiary, are typically involved in the aforementioned etherification and esterification reactions. The use of ethanol and butanol obtained from biomass confers a green character to the derived products. Ethanol can be produced by fermentation of biomass, e.g., corn, grain, and agricultural waste, allowing renewable stock to be introduced into biofuels [19], [20]. Butanol, a potential additive for direct blending to gasoline and a precursor in the synthesis of more-complex molecules, can be produced by fermentation of various carbohydrate substrates [21].

Ion-exchange resins (IERs) used as acid catalysts are promising due to their affordable production, environmentally friendly nature, and ease of reusability. The most widely used acidic IER consists of a polystyrene-divinylbenzene matrix of hydrophobic nature on which sulfo groups (active sites) of hydrophilic nature are anchored. Depending on the porogen used in their manufacture and degree of cross-linking, two main types of resins are distinguished according to their structure: microporous (gel-type) and macroreticular [22, 23]. The former have low-cross-linked closed cells containing micropores and virtually do not show porosity in the dry state. The latter are agglomerates of medium- to highly cross-linked microspheres with spaces between them, which provide permanent porosity to the material (Fig. 1). Anchored sulfo groups (SO_3H) can be either external, i.e., located on the microsphere surface and easily accessible through macropore diffusion, or internal, located within the microspheres with limited accessibility through micropore diffusion [24–27]. Examples of macroreticular resins are Amberlyst™15 (A-15) and its oversulfonated version Amberlyst™35 (A-35). Both can be considered to be reference IERs in heterogeneous catalysis, because of their wide application in fundamental research during the last three decades. Due to the complex nature of IERs, their characterization by spectroscopic and other advanced techniques is rarely found in the literature; thus, the less information available is available compared to other catalysts with well-defined crystalline structure. In spite of such limitations, further effort must be devoted to in situ and ex situ characterization of IERs to reveal structural characteristics at the molecular level and to increase our understanding of these complex materials.

In the catalytic process, compound adsorption on the resin plays a crucial role. Adsorption equilibrium constants appear in the kinetic equation of heterogeneously catalyzed reactions and, therefore, they are usually estimated from the fit of kinetic models to experimental data [28–31]. The weaknesses of such estimations are often the large cross-correlation between different adsorption constants and the fact that the more readily adsorbed compounds can mask the weak adsorption of other species. In addition, from reaction kinetic studies it is usually not possible to separate the diffusion at both levels, through the macropores and within the micropores. Specific adsorption studies allow for better determination of adsorption and diffusion parameters. During the last fifty years, the moment technique has been extensively applied to evaluate adsorption equilibria and rate parameters in chemical reactors, different types of adsorption vessels, and configurations [1, 26, 32–35]. Its foundation and main applications have been highlighted in a recent review [36]. The combination of adsorption studies with the moment technique is a powerful tool for assessing the adsorption equilibrium thermodynamics and the micro- and macropore diffusion kinetics. Surprisingly, experimental data on adsorption equilibrium constants of bioalcohols on IERs is scant [1, 26, 32, 37, 38], especially concerning adsorption rate parameters and effective diffusion coefficients. To the best of our knowledge, the adsorption equilibrium and the diffusivity of BuOH on A-15 in the liquid phase have not yet been investigated. This work aims to shed light on those aspects through the determination of adsorption equilibrium constants, related thermodynamic state functions, and macropore diffusion resistances.

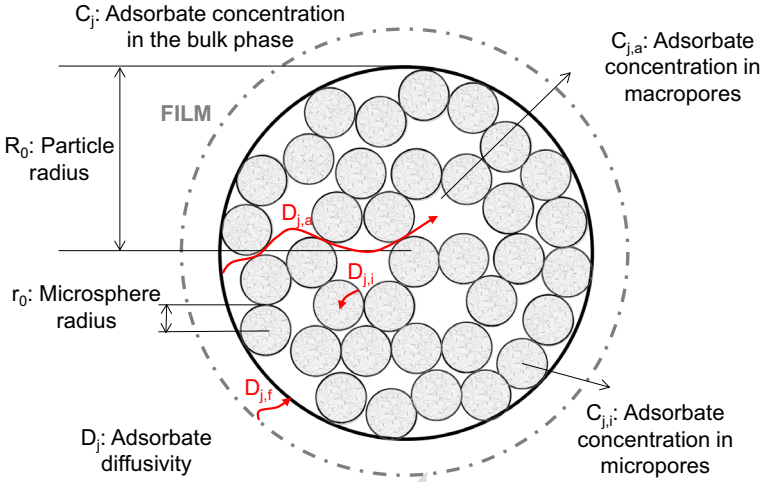

Figure 1. Representation of a macroreticular IER structure with two porosity levels.

2 Experimental Section

The details of the chemicals used, the adsorbent characterization, the experimental setup and procedure for the liquid-phase adsorption experiments can be found in the Supporting Information.

2.1 Theory and Calculations

Diffusion of an adsorbate into the pores of an adsorbent generally determines the adsorption rate of the adsorbed molecules. In a batch adsorber, the species conservation equation of the adsorbing tracer *j* relates the rate of decrease of adsorbate concentration in the bulk phase with the diffusion rate into the pores as follows [Eq. (1)] [32]:

$$\frac{dC_j}{dt} = -\left(\frac{m_s}{\rho_p}\right)\left(\frac{3}{R_0}\right) D_{j,a} \frac{\partial C_{j,a}}{\partial R}\bigg|_{R=R_0} \quad (1)$$

In this adsorption flow model, the n-th moment μ_n[1)] is defined as Eq. (2):

$$\mu_n = \int_0^\infty \left(\frac{C_j - C_{j,eq}}{C_{j,0} - C_{j,eq}}\right) t^n dt \quad (2)$$

In Eqs. (1) and (2), C_j, $C_{j,0}$, and $C_{j,eq}$ are the current, initial, and equilibrium concentrations of the adsorbate in the bulk phase, R_0 is the average adsorbent particle radius, m_s is the ratio of adsorbent dry mass to liquid, ρ_p the adsorbent apparent density, $D_{j,a}$ the macropore effective diffusion coefficient, and n the considered moment. The zeroth moment μ_0 corresponds to the area under the dimensionless concentration-decreasing curve in the batch adsorber and it can be obtained from the experimental concentration data by numerical integration.

For the evaluation of diffusion rates, several models can be proposed assuming perfect mixing, neglecting the external mass transfer resistance of the adsorbate molecules from the bulk phase to the adsorbent surface, and considering linear adsorption (accepted for dilute systems) [32, 35, 36]. In Model A, it is considered that the effective macropore diffusion coefficient $D_{j,a}$ includes the simultaneous contribution of adsorption and Fick diffusion, the macropore diffusion is the rate-controlling step, and thereby the adsorption of the adsorbate is included in the effective diffusivity of this model. In this case, the liquid-phase species conservation equation of the adsorbate can be expressed by equating the adsorbate concentration depletion in the liquid phase to its transport in the adsorbent pores [Eq. (3)]. Conversely, Model B (Eq. (4)) considers that adsorption and diffusion proceed separately. Micropore diffusion resistance is often not significant in the liquid-phase adsorption of alcohols and olefins in IERs, where the efficiency of the adsorbent is mainly governed by the macropore diffusion [1, 32, 39]. In that case, the pseudo-homogeneous species conservation equations are as follows Eqs. (3) and (4):

$$\text{Model A:} \quad \frac{D_{j,a}}{R^2}\frac{\partial}{\partial R}\left(R^2\frac{\partial C_{j,a}}{\partial R}\right) = \frac{\partial C_{j,a}}{\partial t} \quad (3)$$

$$\text{Model B:} \quad \frac{D_{j,a}}{R^2}\frac{\partial}{\partial R}\left(R^2\frac{\partial C_{j,a}}{\partial R}\right) = \left(\varepsilon_a + \rho_p K_j'\right)\frac{\partial C_{j,a}}{\partial t} \quad (4)$$

where the boundary conditions are $\frac{\partial C_{j,a}}{\partial R} = 0$ at $R = 0$, and $C_{j,a} = C_j$ at $R = R_0$.

The solution of Eqs. (3) and (4) in the Laplace domain has been previously reported [32, 33, 35, 40] and the corresponding equations for the zeroth moment for each model are as follows Eqs. (5) and (6):

$$\text{Model A:} \quad \mu_0 = \int_0^\infty \left(\frac{C_j - C_{j,eq}}{C_{j,0} - C_{j,eq}}\right) dt = \frac{R_0^2}{15 D_{j,a}\left(1 + \frac{m_s}{\rho_p}\right)} \quad (5)$$

$$\text{Model B:} \quad \mu_0 = \int_0^\infty \left(\frac{C_j - C_{j,eq}}{C_{j,0} - C_{j,eq}}\right) dt = \frac{R_0^2\left(\varepsilon_A + \rho_p K_j'\right)}{15 D_{j,a}\left(1 + \frac{m_s}{\rho_p}\left(\varepsilon_A + \rho_p K_j'\right)\right)} \quad (6)$$

where ε_A is the adsorbent macroporosity and K'_j the apparent adsorption equilibrium constant of adsorbing species j, which is defined as the product of the maximum adsorption capacity q_m and the liquid-phase adsorption equilibrium constant K_j.

For IER catalysts, diffusion within the microspheres is expected to be strongly influenced by interactions with the polymer matrix, since the adsorbing species are expected to penetrate into the polymeric matrix by forming hydrogen bonds with the SO_3H active sites of the adsorbent. As a result, an approach similar to Model B is a priori more suitable for representing the system [26]. Accordingly, adsorption on the adsorbent external surface is assumed as the first step, followed by diffusion of adsorbed species into the pellet. Hereinafter, the presented results refer to the assessment of the diffusion process described through Model B.

The effective macropore diffusion coefficients $D_{j,a}$ can be estimated by substituting into Eq. (6) the moments obtained by means of numerical integration. In Model B, the previous determination of adsorption equilibrium constants K'_j is required. For highly diluted systems, the adsorption isotherms can be approximated by the Langmuir model Eq. (7) [37]:

$$\frac{q_{eq}}{q_m} = \frac{K_j C_j}{\left(1 + \sum_{j=1}^{S} K_j C_j\right)} \quad (7)$$

where q_{eq} is the adsorbed concentration at equilibrium, defined as $q_{eq}=(C_{j,0}-C_{j,eq})/m_s$, in which m_s is the mass of dry adsorbent divided by the total volume of solid-free liquid ($m_{cat}/V_{T,L}$). The regression of its linear form [Eq. (8)] allows q_m and K_j to be obtained from the slope and the intercept, respectively.

$$\frac{C_j}{q_{eq}} = \frac{1}{K_j q_m} + \frac{C_j}{q_m} \quad (8)$$

For very low tracer concentrations, the term K_jC_j in Eq. (7) becomes much smaller than unity, and therefore q_{eq} can be expressed as $q = q_m K_j C_j$, i.e., a linear relation, justifying thereby the use of Model B. This assumption of linear adsorption is reasonable for dilute systems in which C_{eq} and C_j are sufficiently close. Indeed, it has been already applied in the literature for similar systems, e.g., adsorption of primary alcohols [32], even for higher adsorbate concentrations than those explored herein. Therefore, the used adsorbate concentrations are assumed to be sufficiently low to justify the application of Model B to extract accurate information about macropore diffusion.

When necessary, the dimensionless adsorption equilibrium constant K^*_j can be calculated as Eq. (9):

$$K_j^* = \frac{K_j\left(\rho_{n\text{-heptane}}/MW_j\right)}{\gamma_j} \quad (9)$$

1) List of symbols at the end of the paper.

where γ_j is the activity coefficient of species j at every temperature and composition, $\rho_{n\text{-heptane}}$ the density of n-heptane, and MW_j the molecular weight of adsorbate j.

3 Results and Discussion

3.1 Adsorbent Characterization

The average particle radius of A-15 was determined by laser diffraction in air (Beckman Coulter LS) as 3.25×10^{-4} m. The particle size is not expected to influence the adsorption equilibria (dictated by thermodynamics), but it does affect the rate of filling of the surface by diffusion. The main textural properties extracted from N_2 physisorption are shown in the Supporting Information, including the isotherms obtained for A-15 and A-35 and the corresponding discussion. An apparent density ρ_p [$\rho_p = \rho_e(1\text{-}\varepsilon_A)$] of 0.98 g cm^{-3} was estimated from the skeletal density (ρ_e = 1.416 g cm^{-3}), determined by helium displacement (Accupic 1330), and the porosity (ε_A = 0.317), calculated from N_2 physisorption.

Scanning electron microscopy (SEM) images of crushed particles of A-15 at different magnifications are shown in Fig. 2a–f. High-resolution SEM images were taken in the area perpendicular to the fractured region of crushed spheres (Fig. 2a) to observe properly the inner structure of the adsorbent. The A-15 particles are formed by aggregation of microspheres showing permanent porosity (dark areas), as can be readily seen in Fig. 2b–f at increasing magnification. The particle size distribution of microspheres (Fig. 3) was determined by measuring the particle diameter of more than 350 particles. An average diameter of 62.9 nm was obtained from the geometric mean. Interestingly, this value doubles those previously reported for Amberlyst™18 (30 nm) [41] and A-35 (31.1 nm) [1], which agrees with the larger pore volume and diameter determined for A-15 by N_2 adsorption-desorption (Tab. S2 in the Supporting Information). The observed macropore diameter ranges approximately from 10 to 150 nm, in reasonable agreement with the pore volume reported in Tab. S2. In principle, these pores are large enough to allow the diffusion of n-butanol molecules, the molecular volume of which was estimated as 87.39 Å^3 by using the software Material Studio 2017 (see Sect. S3).

In an attempt to observe morphological features within the adsorbent microspheres, nanoparticles of A-15 were characterized by transmission electron microscopy (TEM). Fig. 2g shows

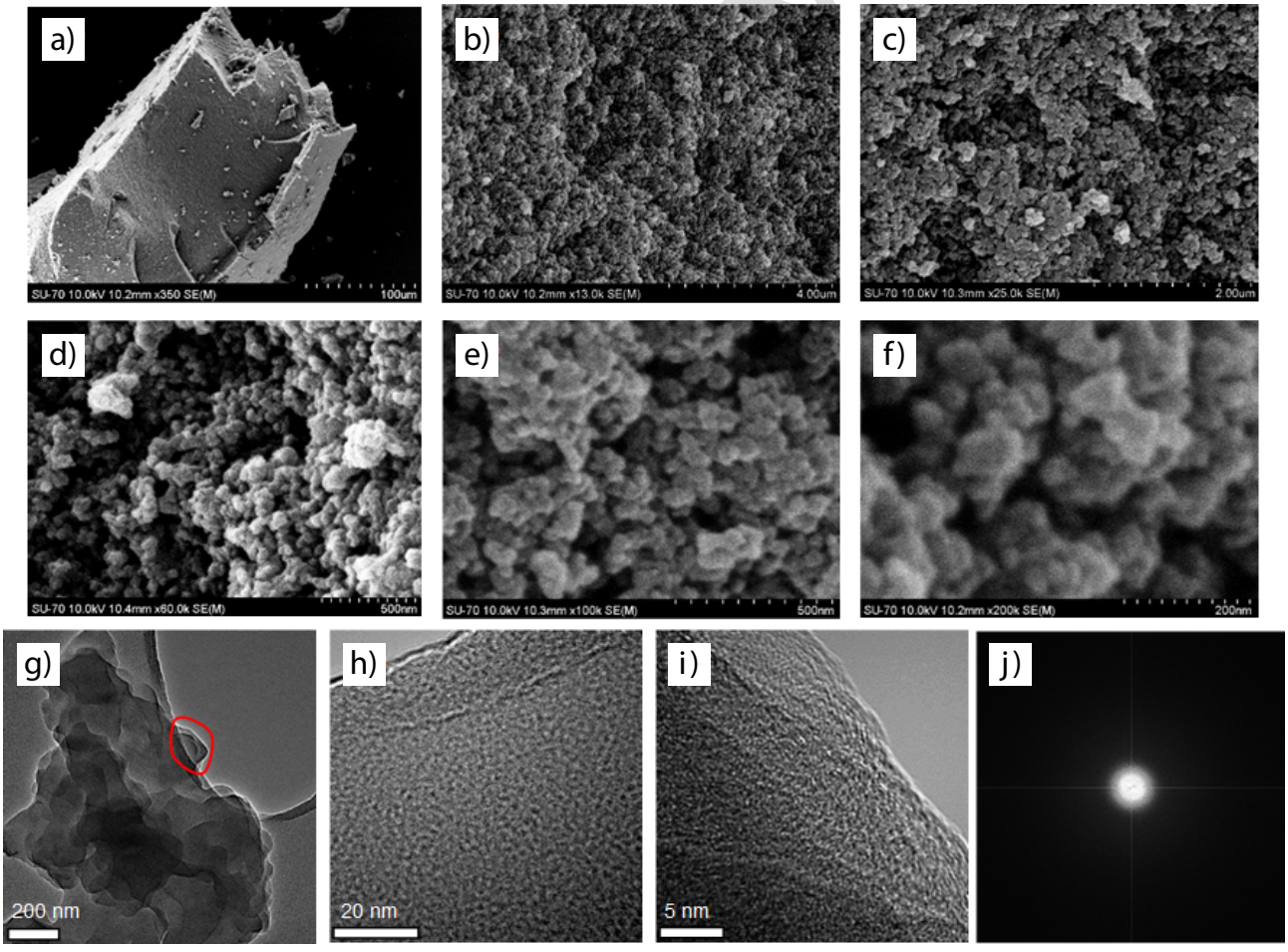

Figure 2. (a)–(f) SEM images of a crushed particle of A-15 at different magnifications. (g)-(i) TEM and high-resolution scanning transmission electron microscopy images of A-15. (j) FFT of image (i).

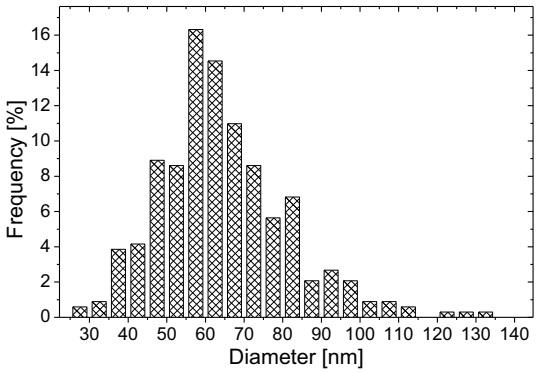

Figure 3. Particle size distribution of microspheres of A-15.

an example of the studied nanoparticles, which are fairly similar to previously reported A-15 nanoparticles [42]. Higher-magnification images on a scale of 5–20 nm (Fig. 2h and i) were taken on the edge of the holey carbon grid used as sample support. The image pattern was similar to that of an amorphous-like carbon, i.e., they do not show a specific shape. The absence of Fresnel fringes reveals the absence of lattice spacing characteristic of crystalline materials, as confirmed by the absence of diffraction rings and spots in the fast Fourier transform (FFT) of the highest-resolution images in Fig. 2j. On the whole, TEM imaging shows an amorphous-like structure of the adsorbent microspheres in which neither the microporosity features nor clusters of sulfo groups can be distinguished due to the agglomeration and overlaying of polymer chains.

Fourier transform infrared (FTIR) analysis of pyridine adsorption was carried out on A-15 and A-35 at 353 K. The full FTIR spectra are shown in Fig. 4a along with the results previously reported [1] for A-35 for comparison. The identification of the main absorption peaks is detailed in the Supporting Information. Moreover, the corresponding solid-state FTIR spectra of A-15 and A-35 catalysts can be found in Sect. S5, wherein differences can hardly be distinguished due to the similar chemical nature of the two adsorbents.

The combination of pyridine adsorption with in situ FTIR spectroscopy can be used to assess the surface acidic properties of supports and catalysts [43] by indicating the type of protonation of pyridine: (1) a pyridinium ion produced by bonding to the nitrogen atom (interaction with Brønsted acid sites) or (2) a pyridinium complex coordinated with unsaturated sites (interaction with Lewis acid sites). The former shows a characteristic band around 1545–1540 cm^{-1}, whereas for the latter the absorption band is located around 1452–1447 cm^{-1}. Absorption bands in between (ca. 1490 cm^{-1}) are typical of both adsorbed species. Magnification of the area of interest in Fig. 4b reveals that acid sites are mostly of Brønsted or Brønsted-Lewis type and the absence of Lewis acid sites. The slightly stronger absorption in these regions for A-35 reveals a more abundant presence of such acid sites than for A-15, whereas the slight shift to lower frequencies of the maximum absorbance for A-15 suggests that molecular interactions are slightly stronger in A-15.

The PXRD patterns obtained for A-15 and A-35 are plotted in Fig. 5. For both resins, in agreement with TEM results, the typical shape of amorphous-like materials, with an absence of sharp and well-defined diffraction peaks, can be distinguished. Both patterns exhibit a broad peak in the 2θ range of 15–22° with maximum at 18° due to the adjacent polymer chains. Very similar results were reported in the literature for A-15 [42], where the presence of the 15–22° peak along with the broad peak between 38 and 45° was attributed to the polyaromatic nature of the materials. The higher intensity reported for A-15 suggests a molecular structure with more structural uniformity and lower degree of disorder than in A-35.

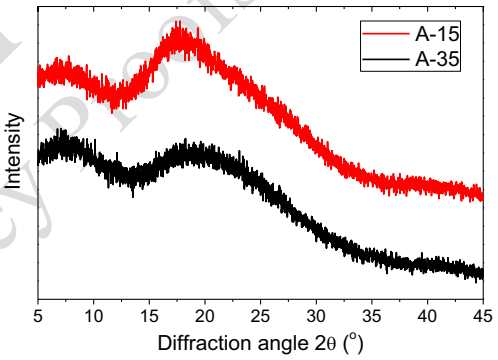

Figure 5. PXRD patterns of crushed A-15 and A-35.

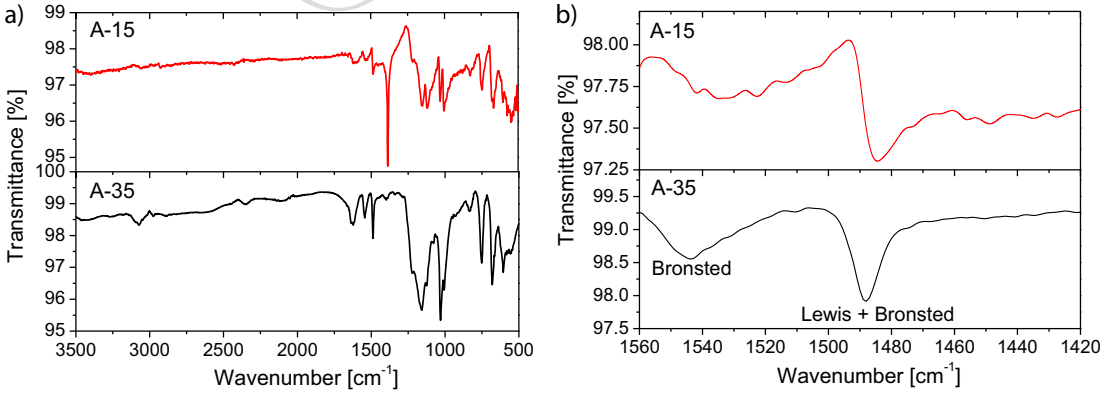

Figure 4. Full spectra (a) and expansion in the area of interest (b) of FTIR spectra for pyridine adsorption at 353 K on A-15 and A-35 adsorbents.

3.2 Liquid-Phase Adsorption Experiments

Fig. 6 shows some examples of the exponential-like decreasing concentration curves obtained at different initial adsorbate (butanol) concentrations. A preliminary experiment was conducted with *n*-hexane as solvent and *n*-heptane as adsorbate to confirm the negligible adsorption of the paraffin on the resin. As expected, the adsorbed butanol concentration ($C_{BuOH,0}$–$C_{BuOH,eq}$) increased with increasing initial adsorbate concentration and decreased with increasing temperature according to the exothermic nature of the adsorption process. At the lowest temperature, the time to reach adsorption equilibrium was inversely proportional to the initial tracer concentration, in agreement with the concentration difference being the driving force.

From the evolution curves, the values of q_{eq} were calculated and used to construct the corresponding Langmuir-type isotherms [Eq. (7)]. Fig. 7 shows illustrative examples of the results obtained, showing that the isotherms have the expected shape and fit accurately the experimental data in their linear form. Tab. 1 summarizes the adsorption equilibrium constants and the maximum adsorption capacities q_m obtained from the fit. The q_m value increases with increasing temperature, while the different expressions of the adsorption equilibrium constants follow the opposite trend, as expected since adsorption is an exothermic process. The activity coefficients for the estimation of K^*_j, which were estimated by using the UNIFAC-Dortmund predictive method [44, 45], were close to unity for *n*-heptane and varied from 15 to 37 (strongly nonideal) for BuOH in the whole range of assayed experimental conditions.

Adsorption equilibrium constants for BuOH on A-15 in the explored range of temperature could not be found in the literature. Our values can be compared only with other studies using a similar adsorbent or adsorbate. As for BuOH adsorption on A-35, the reported adsorption equilibrium constant K_j, apparent adsorption equilibrium constant K'_j, and dimensionless adsorption equilibrium constant K^*_j at 323 K are 21.67 mL mmol^{-1}, 105.7 mL g^{-1}, and 8.67, respectively [1]. These values are slightly higher for A-35, which make sense due to its higher acid capacity and, hence, higher number of active sites. As for EtOH adsorption on A-15, Doğu et al. [37] reported K_{EtOH} = 44.7 mL mmol^{-1} and K'_{EtOH} =407 mL g^{-1} at 306 K, which suggests that EtOH is adsorbed more readily on A-15 than BuOH, in agreement with our published results on the adsorption of both alcohols on A-35 [1]. A possible explanation for this fact relies on the smaller molecular size of EtOH, which allows it to more readily access inner active sites where access of BuOH may be hampered. In addition, the higher polarity of EtOH resulting in stronger interactions with the SO_3H groups and smaller size may also result in a higher number of adsorbed EtOH molecules.

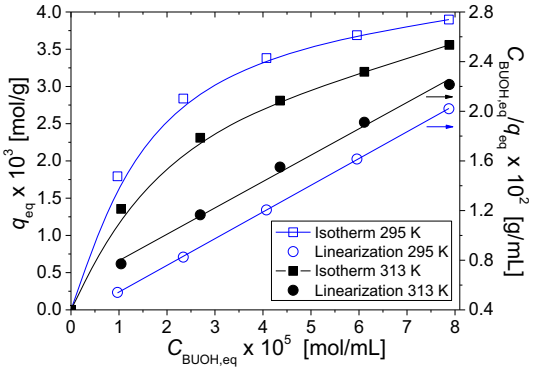

Figure 7. Langmuir-type adsorption isotherms for BuOH on A-15 and their linearization at 295 and 313 K.

Table 1. BuOH adsorption equilibrium constants and parameters from the fit of Langmuir-type isotherms to the experimental data.[a)]

T [K]	q_m [mol g^{-1}]	K_j [mL mmol^{-1}]	K'_j [mL g^{-1}]	K^*_j [–]
323	0.00592	20.45	121.01	8.19
313	0.00471	36.37	171.17	11.27
303	0.00468	46. 90	219.32	12.42
295	0.00466	65.59	304.79	14.46

[a)] $K'_j = K_j \times q_m$ and $K^*_j = K_j \times (\rho_{n\text{-heptane}}/MW_{BuOH})/\gamma_j$.

The van't Hoff plots of K^*_{BuOH} values allowed the estimation of adsorption thermodynamic state functions Eq. (10):

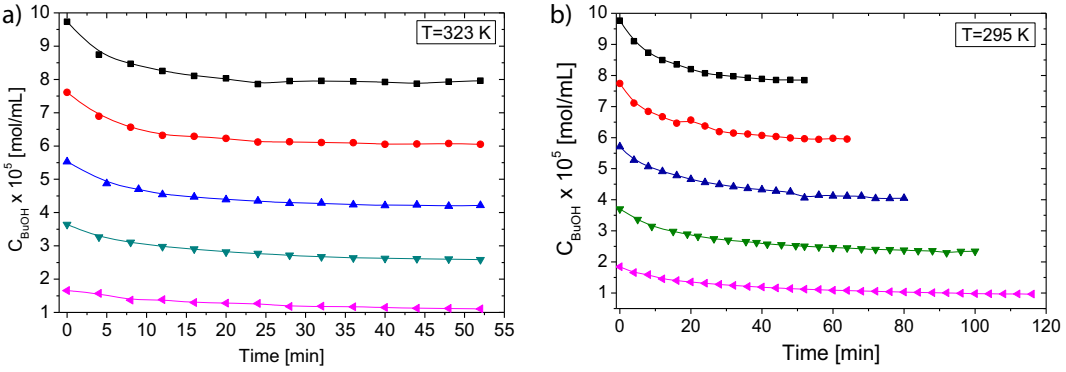

Figure 6. Evolution of the bulk-phase BuOH concentration during its adsorption on A-15 at 295 and 323 K for different initial concentrations.

$$\ln K_j^{*} = \frac{-\Delta_{ads}H_j^{o}}{RT} + \frac{\Delta_{ads}S_j^{o}}{R} \quad (10)$$

where R is the gas constant.

The corresponding plot can be found in Sect. S6, and the goodness of fit is remarkably good (R^2 = 0.97). The liquid-phase adsorption enthalpy $\Delta_{ads}\Delta H^{\circ}_{BuOH}$ and entropy $\Delta_{ads}\Delta S^{\circ}_{BuOH}$ are estimated as (−15.17 ± 2.75) kJ mol^{-1} and (−29.02 ± 8.92) J mol^{-1}K^{-1}, respectively. These figures are larger in absolute value than those reported for the adsorption of BuOH on A-35 in the temperature range 323–353 K [1], i.e., $\Delta_{ads}\Delta H^{\circ}_{BuOH}$ = (−6.9 ± 0.3) kJ mol^{-1} and $\Delta_{ads}\Delta S^{\circ}_{BuOH}$ = (−3.4 ± 1.0) J mol^{-1}K^{-1}. On the one hand, these results confirm the exothermicity of the adsorption of BuOH over A-15. On the other hand, bearing in mind the latent heat of vaporization of BuOH (51.7 kJ mol^{-1}) [46], the released energy indicates that it is a physisorption process, because the heat of adsorption for chemisorption processes is typically 2–3 times larger than the latent heat of vaporization, whereas it is 2–3 times lower for physical adsorption [27]. The larger enthalpy of adsorption obtained for A-15 in comparison to A-35 is consistent with the stronger molecular interactions observed in the pyridine adsorption by FTIR spectroscopy (Fig. 4b).

To assess the thermodynamic consistency of the estimated data, fulfillment of the Boudart rules [47] was also checked. The rules that can be applied to adsorption on IER are: (1) $\Delta_{ads}S^{\circ}_j < 0$, because the adsorption process implies a loss of entropy, (2) $-\Delta_{ads}S^{\circ}_j < S^{\circ}_j$, because the loss of entropy cannot be larger than the total entropy, and (3) $\Delta_{ads}H^{\circ}_j < 0$, because adsorption is an exothermic process. The entropy of formation of BuOH ΔS°_{BuOH} is 225.73 J mol^{-1}K^{-1} [48], much higher than our estimated value of $-\Delta_{ads}\Delta S^{\circ}_{BuOH}$, which along with the negative values of the determined enthalpic and entropic terms confirms the thermodynamic consistency of the estimated data. Within the assayed range of temperature (295–323 K), the Gibbs free energy change ranges from −6.61 to −5.80 kJ mol^{-1}, which confirms that adsorption is spontaneous, and the contribution of the entropic term is about 56–62 % of the enthalpic contribution.

Upon determination of the adsorption equilibrium constants, the moment technique was applied to obtain information about the magnitude of macropore diffusion coefficients $D_{j,a}$. Micropore diffusion resistance can be assumed to be negligible [1, 32]. In the adsorption of other primary alcohols and tertiary olefins over A-15 [32, 39], it was found that the efficiency of the adsorbent operating in liquid-phase reactions is mainly due to the process occurring in the macropores, since the efficiency in the gel microspheres is unity. Dimensionless concentration evolutions, $(C_{BuOH}-C_{BuOH,eq})/(C_{BuOH,0}-C_{BuOH,eq})$ versus time, were calculated, and the zeroth moment [Eq. (2)] was estimated by integration as the area under these curves. Fig. 8 shows some examples of the dimensionless concentration evolutions, which in all cases exhibited an exponential-like decrease of concentration that was slower at lower initial concentration of the adsorbate. The calculated zeroth moments range between 385 and 1587 s, resulting in larger values with decreasing temperatures and adsorbate concentration.

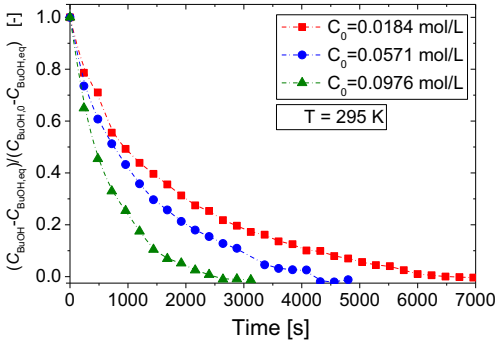

Figure 8. Dimensionless BuOH concentration versus time obtained at 295 K for different initial adsorbent concentrations. Dashed lines are guides to the eye.

By substitution of the calculated zeroth moments in Eq. (6) and using the characterization parameters determined in Sect. 3.1, the macropore diffusion coefficient $D_{BuOH,a}$ was obtained under each set of experimental conditions. Fig. 9 plots the variation of $D_{BuOH,a}$ with the initial adsorbate concentration at the assayed temperatures. The $D_{BuOH,a}$ values range from 1.9×10^{-7} to 2.85×10^{-8} cm s^{-1}, similar to those reported in the literature for EtOH adsorption over A-15 [32] and that of BuOH over A-35 [1]. Diffusion coefficients are strongly influenced by the adsorbate concentration, since $D_{BuOH,a}$ clearly increases with increasing initial concentration of BuOH. These results can be ascribed to a higher initial driving force in the diffusion due to a higher concentration gradient of BuOH. Although the relation of $D_{BuOH,a}$ with temperature is not as clear as in the case of concentration, our reported values somewhat fulfill the expectation by increasing with temperature. However, the influence of concentration on macropore diffusivities is more significant than that of temperature. As comparative figures at 323 K, our $D_{BuOH,a}$ values almost double those previously reported for the diffusion of BuOH on A-35 (ca. 8×10^{-8} cm s^{-1}) [1], which can be explained by the larger surface area, pore volume, and pore diameter of A-15, which are reflected in lower resistance to diffusion through the macropores. Moreover, our values are lower than those report-

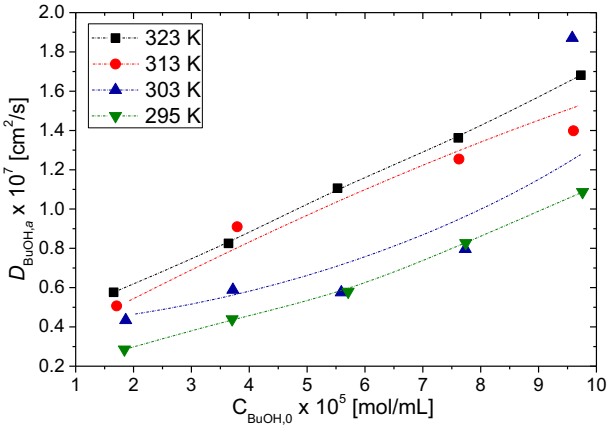

Figure 9. Macropore diffusion coefficients determined as a function of BuOH concentration in the range 295–323 K. Dashed lines are guides to the eye.

ed for the adsorption of methanol and ethanol on A-15 under similar experimental conditions [32], which makes sense due to the lower molecular volume of the adsorbing species and, therefore, lower macropore diffusion resistance.

In our case, lower $D_{BuOH,a}$ values are obtained for higher values of apparent adsorption equilibrium constants K'_j. In a macroporous particle, the relation between surface diffusion D_s and macropore diffusion coefficients is given by Eq. (11):

$$D_{j,a} = D_M \frac{\varepsilon_A}{\tau} + \frac{1}{\tau}\left(\rho_p K_j'\right) D_s \tag{11}$$

where τ is the tortuosity factor, approximated to $1/\varepsilon_A = 3.155$ for A-15, and D_M is the liquid-phase molecular diffusion coefficient of adsorbate j in the solvent. Due to the relatively similar molecular size of the solvent (*n*-heptane) and adsorbate (*n*-butanol), the Wilke-Chang equation [49] was used to calculate molecular diffusivities in diluted binary mixtures rather than the Einstein-Stokes equation [50]. In SI units and accounting for the adsorbate and solvent used in this work, the modified Wilke-Chang equation can be expressed as Eq. (12):

$$D_M = 1.1728 \times 10^{-16} \frac{MW_j T}{\eta_j \left(V_{b,i}\right)^{0.6}} \tag{12}$$

where D_M [$m^2 s^{-1}$] is the molecular diffusivity of *n*-butanol (*i*) in *n*-heptane (*j*), MW_j the molecular weight of *n*-heptane, T [K] the temperature, η_j [Pa s] the *n*-heptane viscosity at the given temperature, and $V_{b,i}$ [$m^3 kmol^{-1}$] the *n*-butanol liquid molar volume at the normal boiling point. Both 4.03×10^{-4} Pa s (295 K) < η_j < 3.05×10^{-4} Pa s (323 K) and $V_{b,i}$ = 31.188 $m^3 kmol^{-1}$ were estimated with the Redlich-Kwong-Soave model by using the software Aspen Plus 11. The final D_M values are in the range (1.08–1.58) × $10^{-11} m^2 s^{-1}$ for the assayed temperatures, about one order of magnitude higher than $D_{j,a}$ values.

In Eq. (11), the first term on the right-hand side refers to the effective molecular diffusivity in the macropores and the second represents the contribution of the surface diffusion. Estimated D_s values increase with temperature and initial *n*-butanol concentration (Fig. 10). Estimated D_s values are notably lower (about 0.6–2.4 %) than $D_{j,a}$, which might indicate an important resistance of surface diffusion, as the slowest step, for the diffusion of molecules through the macropores. Doğu et al. [32] reported surface diffusion contributions in the range 2–9 % for smaller molecules, e.g., methanol and ethanol, in A-15, with a significant contribution of surface diffusion.

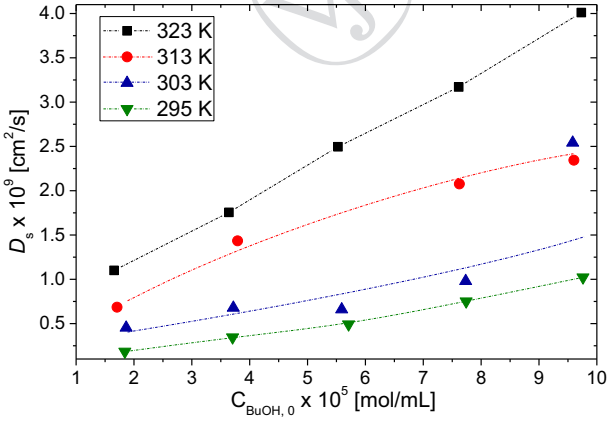

Figure 10. Estimated D_s values from Eq. (11) as a function of BuOH concentration in the range 295–323 K. Dashed lines are guides to the eye.

4 Conclusion

Although the amount of information that can be extracted by FTIR spectroscopy and PXRD for ion-exchange resins is limited, it allows some interesting inferences and comparison between resins. The active sites of A-15 and A-35 resins are of Brønsted or Brønsted-Lewis type and the structure of A-15 shows more structural regularity than that of A-35. The moment technique was successfully applied to study the liquid-phase adsorption of *n*-butanol on A-15. From Langmuir isotherm linearization, the maximum adsorption capacity and the liquid-phase adsorption equilibrium constants could be estimated at any temperature within the assayed range. In agreement with the exothermicity of the process, the adsorption equilibrium constants decrease with increasing temperature. The estimated values are in good agreement with previously reported results for A-35. The thermodynamic state functions were estimated by van't Hoff plot of adsorption equilibrium constants, resulting in $\Delta_{ads}\Delta H°_{BuOH}$ = (−15.17 ± 2.75) kJ mol^{-1} and $\Delta_{ads}\Delta S°_{BuOH}$ = (−29.01 ± 8.92) J $mol^{-1}K^{-1}$, which suggest physical adsorption of the adsorbate under the explored conditions. The results are thermodynamically consistent and fulfil the Boudart rules. By the moment technique, the estimated macropore diffusion coefficient $D_{j,a}$ of *n*-butanol on A-15 ranges from 1.9×10^{-7} to 2.85×10^{-8} cm s^{-1}. These values are higher than those reported for A-35 in BuOH under comparable conditions, which can be explained by the larger surface area, pore volume, and diameter of A-15. Macropore effective diffusion coefficients and surface diffusion coefficients D_s generally increased with increasing temperature and initial concentration of BuOH (larger driving force). The results are consistent with a significant contribution of the surface diffusion resistance to the macropore diffusion, since estimated D_s values are about two orders of magnitude lower than $D_{j,a}$. The obtained values from the performed equilibrium and kinetic analyses could be used to predict concentration decay curves in the batch adsorber by means of the evaluated diffusion model.

Supporting Information

Supporting Information for this article can be found under DOI: 10.1002/ceat.202100253. This section includes additional references to primary literature relevant for this research [51–56].

Data Availability Statement

■Data available on request from the authors.■

Acknowledgement

The authors are grateful to Rohm & Haas France SAS (The Dow Chemical Company) for providing the ion-exchange resin Amberlyst™35 and to the Gazi University (Ankara) and the University of Limerick (Ireland) for providing the facilities to perform the experimental work. Thanks to Laura González Saladich for the artwork contribution to the graphical abstract. Finally, the authors gratefully acknowledge Prof. Timur Doğu and Prof. Dr. Gülsen Doğu for their valuable contributions.

The authors have declared no conflict of interest.

Symbols used

C_j	[mol L^{-1}]	adsorbate concentration in the bulk phase (liquid)
$C_{j,0}$	[mol L^{-1}]	initial concentration of adsorbate *j*
$C_{j,a}$	[mol L^{-1}]	concentration of adsorbate *j* in macopores
$C_{j,eq}$	[mol L^{-1}]	equilibrium concentration of adsorbate *j*
$C_{j,i}$	[mol L^{-1}]	concentration of adsorbate *j* in micropores
D_0	[m]	average diameter of adsorbent particles
$D_{j,a}$	[m^{2}s^{-1}]	effective macropore diffusion coefficient of adsorbate *j*
$D_{j,f}$	[m^{2}s^{-1}]	effective film diffusion coefficient of adsorbate *j*
$D_{j,i}$	[m^{2}s^{-1}]	effective micropore diffusion coefficient of adsorbate *j*
D_M	[m^{2}s^{-1}]	molecular diffusivity of adsorbate in the solvent
D_s	[m^{2}s^{-1}]	surface diffusion coefficient
$\Delta_{ads}H^\circ_j$	[kJ mol^{-1}]	standard molar heat of adsorption of compound *j*
$\Delta_{ads}S^\circ_j$	[J mol^{-1}K^{-1}]	standard molar entropy of adsorption of compound *j*
ΔS°_j	[J mol^{-1}K^{-1}]	entropy of formation of compound *j*
K_j	[m^{3}kg^{-1}]	adsorption equilibrium constant of compound *j*
$K^\star_j$	[–]	dimensionless adsorption equilibrium constant of compound *j*
K'_j	[m^{3}kg^{-1}]	apparent adsorption equilibrium constant of compound *j*
m_{cat}	[g]	mass of dry adsorbent
m_s	[–]	ratio of adsorbent dry mass to liquid
MW_j	[g mol^{-1}]	molecular weight of compound *j*
q	[mmol g^{-1}]	adsorbed concentration
q_{eq}	[mmol g^{-1}]	adsorbed concentration at adsorption equilibrium
q_m	[mmol g^{-1}]	maximum adsorption capacity (at saturation)
r_0	[m]	average micrograin radius
R	[J K^{-1}mol^{-1}]	gas constant
R_0	[m]	average radius of adsorbent particles
$V_{b,i}$	[m^{3}kmol^{-1}]	*n*-butanol liquid molar volume at the normal boiling point
$V_{T,L}$	[m^3]	total volume of solid-free liquid

Greek letters

■ε_a	[–]	macroporosity of the adsorbent
μ_n	■	*n*-th moment
ρ_e	[kg m^{-3}]	skeletal density
ρ_p	[kg m^{-3}]	adsorbent apparent density
γ_j	[–]	activity coefficient of a species *j*
τ	[–]	macropore tortuosity factor
η_j	[Pa s]	*n*-heptane (solvent) viscosity at the given temperature

Abbreviations

A-15	Amberlyst™15
A-35	Amberlyst™35
IER	ion-exchange resin
FFT	fast Fourier transform
FTIR	Fourier transform infrared
SEM	Scanning electron microscopy
TEM	transmission electron microscopy

References

[1] R. Soto, N. Oktar, C. Fité, E. Ramírez, R. Bringué, J. Tejero, *Chem. Eng. Technol.* **2017**, *40 (5)*, 889–899. DOI: https://doi.org/10.1002/ceat.201600592

[2] M. A. Pérez, R. Bringué, M. Iborra, J. Tejero, F. Cunill, *Appl. Catal. A Gen.* **2014**, *482*, 38–48. DOI: https://doi.org/10.1016/j.apcata.2014.05.017

[3] K. C. Maheria, J. Kozinski, A. Dalai, *Catal. Lett.* **2013**, *143 (11)*, 1220–1225. DOI: https://doi.org/10.1007/s10562-013-1041-3

[4] "2050 long-term strategy | Climate Action." https://ec.europa.eu/clima/policies/strategies/2050_en (accessed Jan. 20, 2020).

[5] J. H. Badia, C. Fité, R. Bringué, M. Iborra, F. Cunill, *Top. Catal.* **2015**, *58*, 919–932. DOI: https://doi.org/10.1007/s11244-015-0460-3

[6] J. H. Badia, C. Fité, R. Bringué, E. Ramírez, J. Tejero, *Appl. Catal. A Gen.* **2017**, *541*, 141–150. DOI: https://doi.org/10.1016/J.APCATA.2017.04.006

[7] R. Bringué, J. Tejero, M. Iborra, J. F. Izquierdo, C. Fité, F. Cunill, *Ind. Eng. Chem. Res.* **2007**, *46 (21)*, 6865–6872. DOI: https://doi.org/10.1021/ie0616646

[8] J. Guilera, E. Ramírez, C. Fité, J. Tejero, F. Cunill, *Catal. Sci. Technol.* **2015**, *5 (4)*, 2238–2250. DOI: https://doi.org/10.1039/C4CY01548G

[9] J. Guilera, R. Bringué, E. Ramírez, M. Iborra, J. Tejero, *Appl. Catal. A Gen.* **2012**, *413–414*, 21–29. DOI: https://doi.org/10.1016/j.apcata.2011.10.037

[10] W. Kiatkittipong, S. Suwanmanee, N. Laosiripojana, P. Praserthdam, S. Assabumrungrat, *Fuel Process. Technol.* **2009**, *91 (5)*, 456–460. DOI: https://doi.org/10.1016/j.fuproc.2009.12.004

[11] B. Ikizer, N. Oktar, T. Doğu, *Fuel Process. Technol.* **2015**, *138*, 570–577. DOI: https://doi.org/10.1016/J.FUPROC.2015.06.039

[12] J. F. Izquierdo, M. Montiel, I. Palés, P. R. Outón, M. Galán, L. jutglar, M. Vilarrubia, M. Izquierdo, M. P. Hermo, X. Ariza, *Renewable Sustainable Energy Rev.* **2012**, *16 (9)*, 6717–6724. DOI: https://doi.org/10.1016/J.RSER.2012.08.005
[13] D. Mravec, A. Turan, A. Filková, N. Mikesková, E. Volkovicsová, G. Onyestyák, S. harnos, F. Lónyi, J. Valyon, A. Kaszonyi, *Fuel Process. Technol.* **2017**, *159*, 111–117. DOI: https://doi.org/10.1016/J.FUPROC.2017.01.012
[14] F. Frusteri, F. Arena, G. Bonura, C. Cannilla, L. Spadaro, O. Di Blasi, *Appl. Catal. A Gen.* **2009**, *367 (1–2)*, 77–83. DOI: https://doi.org/10.1016/J.APCATA.2009.07.037
[15] M. A. Tejero, E. Ramírez, C. Fité, J. Tejero, F. Cunill, *Appl. Catal. A Gen.* **2016**, *517*, 56–66. DOI: https://doi.org/10.1016/j.apcata.2016.02.032
[16] C. R. Patil, P. S. Niphadkar, V. V. Bokade, P. N. Joshi, *Catal. Commun.* **2014**, *43*, 188–191. DOI: https://doi.org/10.1016/J.CATCOM.2013.10.006
[17] D. R. R. Fernandes, A. S. S. Rocha, E. F. F. Mai, C. J. A. Mota, V. Teixeira da Silva, *Appl. Catal. A Gen.* **2012**, *425–426*, 199–204. DOI: https://doi.org/10.1016/j.apcata.2012.03.020
[18] A. Garcia-Ortiz, K. S. Arias, M. J. Climent, A. Corma, S. Iborra, *ChemSusChem* **2020**, *13 (4)*, 707–714. DOI: https://doi.org/10.1002/cssc.201903496
[19] L. R. Lynd, J. H. Cushman, R. J. Nichols, C. E. Wyman, *Science* **1991**, *251 (4999)*, 1318–1323. DOI: https://doi.org/10.1126/science.251.4999.1318
[20] S. Radhakrishnan, J. Franken, J. A. Martens, *Green Chem.* **2012**, *14 (5)*, 1475–1479. DOI: https://doi.org/10.1039/c2gc35220f
[21] R. Cascone, *Chem. Eng. Prog.* **2008**, *108 (8)*, 54–59.
[22] S.-K. Ihm, J.-H. Ahn, Y.-D. Jo, *Ind. Eng. Chem. Res.* **1996**, *35 (9)*, 2946–2954. DOI: https://doi.org/10.1021/ie950724x
[23] R. L. Albright, *React. Polym. Ion Exch. Sorbents* **1986**, *4 (2)*, 155–174. DOI: https://doi.org/10.1016/0167-6989(86)90010-3
[24] G. Doğu, C. Ercan, *Can. J. Chem. Eng.* **1983**, *61 (5)*, 660–664. DOI: https://doi.org/10.1002/cjce.5450610507
[25] N. Hashimoto, J. M. Smith, *Ind. Eng. Chem. Fundam.* **1974**, *13 (2)*, 115–120. DOI: https://doi.org/10.1021/i160050a005
[26] N. Oktar, K. Mürtezaoğlu, G. Doğu, T. Doğu, *Can. J. Chem. Eng.* **1999**, *77 (2)*, 406–412. DOI: https://doi.org/10.1002/cjce.5450770229
[27] D. M. Ruthven, *Principles of Adsorption and Adsorption Processes*, 1st ed., John Wiley & Sons, New York **1984**.
[28] M. Á. Pérez-Maciá, R. Bringué, M. Iborra, J. Tejero, F. Cunill, *AIChE J.* **2016**, *62 (1)*, 180–194. DOI: https://doi.org/10.1002/aic.15020
[29] J. Guilera, R. Bringué, E. Ramírez, C. Fité, J. Tejero, *AIChE J.* **2014**, *60 (8)*, 2918–2928. DOI: https://doi.org/10.1002/aic.14497
[30] R. Soto, C. Fité, E. Ramírez, R. Bringué, F. Cunill, *Chem. Eng. J.* **2017**, *307*, 22–134. DOI: https://doi.org/10.1016/j.cej.2016.08.038
[31] J. H. Badia, C. Fité, R. Bringué, M. Iborra, F. Cunill, *Chem. Eng. J.* **2019**, *356*, 219–226. DOI: https://doi.org/10.1016/J.CEJ.2018.08.153
[32] T. Doğu, E. Aydin, N. Boz, K. Murtezaoglu, G. Doğu, *Int. J. Chem. React. Eng.* **2003**, *1 (1)*, 1–10. DOI: https://doi.org/10.2202/1542-6580.1012
[33] T. Furusawa, M. Suzuki, *J. Chem. Eng. Jpn.* **1975**, *8 (2)*, 119–122. DOI: https://doi.org/10.1252/jcej.8.119
[34] D. Varisli, T. Doğu, *Ind. Eng. Chem. Res.* **2005**, *44 (14)*, 5227–5232. DOI: https://doi.org/10.1021/ie049241w
[35] J. Yener, T. Kopac, G. Doğu, T. Doğu, *Chem. Eng. J.* **2008**, *144 (3)*, 400–406. DOI: https://doi.org/10.1016/J.CEJ.2008.02.009
[36] G. Doğu, T. Doğu, *Int. J. Chem. React. Eng.* **2019**, *17 (5)*, 20180142. DOI: https://doi.org/10.1515/ijcre-2018-0142
[37] T. Doğu, N. Boz, E. Aydin, N. Oktar, K. Mürtezaoğlu, G. Doğu, *Ind. Eng. Chem. Res.* **2001**, *15*, 5044–5051. DOI: https://doi.org/10.1021/ie000922a
[38] P. M. Słomkiewicz, *J. Chromatogr. A* **2004**, *1034 (1–2)*, 169–174. DOI: https://doi.org/10.1016/j.chroma.2004.01.036
[39] R. M. Quinta Ferreira, C. A. Almeida-Costa, A. E. Rodrigues, *Ind. Eng. Chem. Res.* **1996**, *35 (11)*, 3827–3841. DOI: https://doi.org/10.1021/ie9602421
[40] J. Yener, T. Kopac, G. Doğu, T. Doğu, *Sep. Sci. Technol.* **2006**, *41 (9)*, 1857–1879. DOI: https://doi.org/10.1080/01496390600674851
[41] N. S. Caetano, J. M. Loureiro, A. E. Rodrigues, *Chem. Eng. Sci.* **1994**, *49 (24)*, 4589–4604. DOI: https://doi.org/10.1016/S0009-2509(05)80043-0
[42] N. T. Le, P. Lakshmanan, K. Cho, Y. Han, H. Kim, *Appl. Catal. A Gen.* **2013**, *464–465*, 305–312. DOI: https://doi.org/10.1016/j.apcata.2013.06.002
[43] D. Li, P. Bui, H. Y. Zhao, S. T. Oyama, T. Dou, Z. H. Shen, *J. Catal.* **2012**, *290*, 1–12. DOI: https://doi.org/10.1016/j.jcat.2012.02.001
[44] J. Gmehling, J. Li, M. Schiller, *Ind. Eng. Chem. Res.* **1993**, *32 (1)*, 178–193. DOI: https://doi.org/10.1021/ie00013a024
[45] J. Gmehling, J. Lohmann, A. Jakob, J. Li, R. Joh, *Ind. Eng. Chem. Res.* **1998**, *37 (12)*, 4876–4882. DOI: https://doi.org/10.1021/ie980347z
[46] T. Schmeling, R. Strey, *Ber. Bunsenges. Phys. Chem.* **1983**, *87 (10)*, 871–874. DOI: https://doi.org/10.1002/bbpc.19830871008
[47] M. V. M. Boudart, D. E. Mears, *Ind. Chim. Belge* **1967**, *32*, 281–284.
[48] J. F. Counsell, J. L. Hales, J. F. Martin, *Trans. Faraday Soc.* **1965**, *61*, 1869–1875. DOI: https://doi.org/10.1039/tf9656101869
[49] C. R. Wilke, P. Chang, *AIChE J.* **1955**, *1 (2)*, 264–270. DOI: https://doi.org/10.1002/aic.690010222
[50] H. A. Kooijman, *Ind. Eng. Chem. Res.* **2002**, *41 (13)*, 3326–3328. DOI: https://doi.org/10.1021/ie010690v
[51] S. Lowell, J. E. Shields, S. Lowell, J. E. Shields, Powder Surface Area and Porosity Introduction, in *Powder Surface Area and Porosity*, Springer, Berlin **1991**, 3–6.
[52] G. Leofanti, M. Padovan, G. Tozzola, B. Venturelli, *Catal. Today* **1998**, *41 (1–3)*, 207–219. DOI: https://doi.org/10.1016/S0920-5861(98)00050-9
[53] M. Umar, D. Patel, B. Saha, *Chem. Eng. Sci.* **2009**, *64 (21)*, 4424–4432. DOI: https://doi.org/10.1016/j.ces.2009.07.015
[54] R. Soto, C. Fité, E. Ramírez, M. Iborra, J. Tejero, *React. Chem. Eng.* **2018**, *3 (2)*, 195–205. DOI: https://doi.org/10.1039/c7re00177k
[55] K. Jeřábek, *Anal. Chem.* **1985**, *57 (8)*, 595–1597. DOI: https://doi.org/10.1021/ac00285a022
[56] F. Mü, C. A. Ferreira, L. Franco, J. Puiggalí, C. Alema, E. Armelin, *J. Phys. Chem. B.* **2012**, *116 (38)*, 11767–11779. DOI: https://doi.org/10.1021/jp3068415

Research Article: Esters obtained from biomass-derived ketoacids and alcohols such as *n*-butanol in the presence of an acid catalyst such as Amberlyst™35 resin are potential biofuels and platform chemicals. The thermodynamics of the liquid-phase adsorption equilibrium of *n*-butanol on Amberlyst™35 were determined and used in combination with the moment technique to estimate effective macropore diffusivities.

Experimental Study on the Liquid-Phase Adsorption Equilibrium of *n*-Butanol over Amberlyst™15 and Contribution of Diffusion Resistances

Rodrigo Soto*,Nuray Oktar, Carles Fité, Eliana Ramirez, Roger Bringué, Javier Tejero

Chem. Eng. Technol. **2021**, *44 (12)*, XXX … XXX

DOI: 10.1002/ceat.202100253

Supporting Information available online